

1 **Lightning-generated NO_x seen by OMI during NASA's TC⁴ experiment**

2 Eric J. Bucsel¹, Kenneth E. Pickering², Tabitha L. Huntemann³, Ronald C. Cohen⁴, Anne
3 Perring⁴, James F. Gleason², Richard J. Blakeslee⁵, Rachel I. Albrecht³, Robert Holzworth⁶,
4 James P. Cipriani³, Dylana Vargas-Navarro⁷, Ileana Mora-Segura⁷, Alexia Pacheco-Hernández⁷,
5 Sadí Laporte-Molina⁷

6

7 ¹SRI International,

8 ²NASA Goddard Space Flight Center,

9 ³University of Maryland,

10 ⁴University of California, Berkeley,

11 ⁵NASA Marshall Space Flight Center,

12 ⁶University of Washington,

13 ⁷Instituto Costarricense de Electricidad

14 **Abstract:** We present case studies identifying lightning-generated upper-tropospheric NO_x
15 (LNO_x) observed during NASA's Tropical Composition, Cloud and Climate Coupling
16 Experiment (TC⁴) in July and August 2007. In the campaign, DC-8 aircraft missions, flown from
17 Costa Rica, recorded *in situ* NO₂ profiles near active storms and in relatively quiet areas. We
18 combine these TC⁴ DC-8 data with satellite data from the Ozone Monitoring Instrument (OMI)
19 to estimate the lightning-generated NO₂ (LNO₂)—above background levels—in the observed
20 OMI NO₂ fields. We employ improved off-line processing techniques to customize the OMI
21 retrieval for LNO₂. Information on lightning flashes—primarily cloud-to-ground (CG)—
22 observed by the Costa Rica Lightning Detection Network (CRLDN - operated by the Instituto
23 Costarricense de Electricidad) and the World Wide Lightning Location Network (WWLLN)
24 were examined over storms upwind of regions where OMI indicates enhanced LNO₂. These flash
25 data are compared with Tropical Rainfall Measuring Mission/Lightning Imaging Sensor
26 (TRMM/LIS) satellite data to estimate total flashes. Finally, using [NO₂]/[NO_x] ratios from
27 NASA's Global Modeling Initiative model, we estimate LNO_x production per flash for four
28 cases and obtain rates of ~100–250 mol/flash. These are consistent with rates derived from
29 previous studies of tropical and subtropical storms, and below those from modeling of observed
30 mid-latitude storms. In our study, environments with stronger anvil-level winds were associated
31 with higher production rates. LIS flash footprint data for one of the low-LNO_x production cases
32 with weak upper tropospheric winds suggest below-average flash lengths for this storm. LNO_x
33 enhancements over background determined from the OMI data were in less than, but roughly
34 proportional to aircraft estimates.

35

35 **1. Introduction**

36

37 NO₂ and NO (together referred to as NO_x) are trace gases important in ozone chemistry in both
38 the troposphere and stratosphere. Worldwide, anthropogenic emissions of NO_x dominate the NO_x
39 budget. However, considerable uncertainty surrounds emission rates from natural sources
40 (lightning and soil). Lightning is the largest non-anthropogenic source of NO_x in the free
41 troposphere (hereafter, we refer to lightning-generated NO_x as LNO_x). The most accepted
42 estimates of global LNO_x production range from 2 to 8 Tg (N) yr⁻¹ [*Schumann and Huntrieser,*
43 2007], or about 10–15% of the total NO_x budget. The effects of lightning are felt most strongly
44 in the middle and upper part of the troposphere, where this source plays the dominant role in
45 controlling NO_x and ozone amounts, despite the greater overall magnitude of the anthropogenic
46 NO_x emissions [*R. Zhang et al., 2003*]. In this region, NO_x has a lifetime of 5–10 times longer
47 than the approximate 1-day lifetime in the lower troposphere [*Jaeglé et al., 1998; Martin et al.,*
48 2007] so that a given amount of LNO_x in the upper troposphere can have a greater impact on
49 ozone chemistry. Ozone production can proceed at rates of up to 10 ppbv per day in the
50 lightning-enhanced convective outflow plumes of ozone precursors [*DeCaria et al., 2005; Ott et*
51 *al., 2007; Pickering et al., 1996*]. Ozone is the third most important greenhouse gas, and ozone
52 enhancements near the tropopause have the greatest effect on its radiative forcing. Therefore,
53 additional ozone produced downwind of thunderstorm events is particularly effective in climate
54 forcing.

55

56 Recent studies have attempted to constrain the magnitude of the global LNO_x source using
57 satellite observations. *Bond et al.* [2002] combined satellite measurements of lightning with
58 models based on climatological parameterizations of LNO_x production to infer a global
59 production rate of 6.3 Tg (N) yr⁻¹. Other studies have used satellite measurements of NO₂
60 directly in their calculations. *Beirle et al.* [2004] used Global Ozone Monitoring Instrument
61 (GOME) NO₂ column densities over Australia and data from the Lightning Imaging Sensor
62 (LIS) to estimate that lightning produces 2.8 Tg (N) yr⁻¹, but the range of uncertainty was large
63 (0.8–14 Tg (N) yr⁻¹). *Beirle et al.* [2006] studied LNO_x production from a storm system in the
64 Gulf of Mexico using GOME data and National Lightning Detection Network (NLDN)
65 observations. Extrapolating their findings to the global scale, they estimated an LNO_x source of
66 1.7 Tg (N) yr⁻¹ with a range of uncertainty from 0.6 to 4.7 Tg (N) yr⁻¹. *Boersma et al.* [2005]
67 used GOME NO₂ observations and the TM3 global chemical transport model with two different
68 LNO_x parameterizations and concluded that LNO_x production was between 1.1 and 6.4 Tg (N)
69 yr⁻¹. In their study, stratospheric NO₂ was estimated and removed from the data by an
70 assimilation approach using the TM3 model. *Martin et al.* [2007] used Goddard Earth Observing
71 System chemistry model (GEOS-Chem) simulations in conjunction with space-based
72 observations of NO_x, ozone, and nitric acid to estimate LNO_x production of 6 ± 2 Tg (N) yr⁻¹.
73 Their NO₂ data were obtained using the Scanning Imaging Absorption Spectrometer for
74 Atmospheric Cartography/chemistry (SCIAMACHY) instrument and analyzed with methods
75 similar to those described in *Martin et al.* [2002]. In general, satellite observations of LNO_x are
76 challenging because of issues of cloud cover and because most upper tropospheric NO_x exists in
77 the form of NO, which is not directly detectable from space. *Beirle et al.* [2009] have
78 demonstrated, through the use of cloud/chemistry and radiative transfer modeling, that nadir-

79 viewing satellites likely have a sensitivity near or less than 50% for LNO_x produced in a typical
80 marine convective system. Therefore, when satellite data are used to estimate LNO_x, this
81 sensitivity factor must be taken into account.

82
83 A critical quantity in many studies that attempt to infer global production rates is the rate of NO_x
84 generation in individual thunderstorms, often expressed as the number of moles of NO_x produced
85 per lightning flash. Estimates for this NO_x generation can vary by at least an order of magnitude
86 [Zhang *et al.*, 2003], with many estimates between 50 and 700 mol/flash [Ott *et al.*, 2007, 2009
87 and references therein]. From studies of individual storms, these estimates have been
88 extrapolated to provide global LNO_x production rates. However, such extrapolations are
89 complicated by variations in pressure-level, intensity, and length of lightning strokes for tropical
90 versus mid-latitude storms. The satellite investigation by Beirle *et al.* [2006] found that, on
91 average, lightning in the Gulf of Mexico system produced 90 mol/flash NO. Modeling studies
92 [e.g., Ott *et al.*, 2009] have examined how these parameters vary for intracloud (IC) and cloud-
93 to-ground (CG) flashes in different latitude regions. The variations may result in different LNO_x
94 production rates, P_{IC} and P_{CG}, for IC and CG flashes, respectively. Although early investigations
95 [e.g., Price *et al.*, 1997] suggest that the value of the ratio P_{IC}/P_{CG} is much less than 1 (~0.1),
96 more recent studies provide evidence that the value may be near unity or even greater [DeCaria
97 *et al.*, 2005; Fehr *et al.*, 2004; Ott *et al.*, 2007, 2009; Zhang *et al.*, 2003]. Huntrieser *et al.* [2008]
98 suggest that overall production of LNO_x per flash, P_{IC+CG}, may be 2–8 times larger in subtropical
99 and mid-latitude storms than in tropical storms. This result may be due to longer flash channel
100 lengths outside the tropics in regions of greater vertical wind shear.

101

102 In this paper we examine four tropical convective events from the NASA Tropical Composition,
103 Clouds, and Climate Coupling (TC⁴) campaign [Toon *et al.*, 2009] and compute the number of
104 moles of LNO_x per flash using a combination of data from the Ozone Monitoring Instrument
105 (OMI) instrument on the Aura satellite, *in situ* observations from the DC-8 aircraft, global
106 chemical transport model output, and ground-based lightning flash observations. Our approach
107 differs from those of previous satellite investigations in the methods used to remove the
108 stratospheric and tropospheric background (as described later in this paper), and because we
109 derive LNO_x production per flash directly from an estimate of accumulated LNO_x and lightning
110 flash counts, rather than by adjusting model parameters to match the satellite data. Our use of
111 OMI data is better suited to individual case studies than are the lower-resolution GOME and
112 SCIAMACHY data. We also focus exclusively on tropical-latitude storms that occurred over
113 ocean regions. In these regions convection is less tied to late-afternoon diurnal cycles (and hence
114 more likely to occur before or near the OMI overpass time of ~13:45 local time [LT]), and NO₂
115 contamination from anthropogenic sources is less [Beirle *et al.*, 2009]. We use measured OMI
116 NO₂ columns and CG flash counts. From these we estimate the LNO_x columns and the total
117 flashes (IC + CG) and combine results to obtain the P_{CG+IC} for the storms on the 4 days studied.
118 We then examine our results in the context of estimates of LNO_x per flash from other studies.

119

120 Section 2 describes the data we used in our analyses. Section 3 details the calculations that were
121 performed in the LNO_x retrieval process and describes how we used the retrieved LNO_x values,
122 in combination with flash rates, to estimate production per flash. Results are presented in Section
123 4. We discuss the implications of the derived values and their uncertainties in Section 5 and draw
124 conclusions in Section 6.

125

126 **2. Data Overview**

127

128 **2.1 TC⁴: Aircraft measurements and lightning data**

129

130 During July and August 2007, NASA launched the TC⁴ experiment to study a variety of
131 atmospheric physical and chemical processes in the Eastern Pacific and other areas near Costa
132 Rica. Among TC⁴ objectives was validation of measurements from OMI, including cloud
133 properties and column amounts of the trace gases ozone, NO₂, and SO₂. NO and NO₂
134 measurements at a variety of altitudes near tropical convection were also intended to assess the
135 lightning NO_x budget. In this study, we used *in situ* NO₂ measurements from the University of
136 California at Berkeley's laser-induced fluorescence instrument [Thornton *et al.*, 2000, 2003]
137 onboard the NASA DC-8 aircraft, which flew in and around thunderstorms and also sampled
138 relatively undisturbed air in "clean" areas of the Pacific and Caribbean. Figure 1 shows partial
139 DC-8 flight tracks for the sampling within and near convective systems on July 17, 21, and 31,
140 and on August 5.

141

142 Observed lightning flashes near the storms of interest were counted so that the per-flash
143 production rates of LNO_x could be determined. In this study, we use flash data from ground-
144 based detectors of the local Costa Rica Lightning Detection Network (CRLDN) and the global
145 scale Worldwide Lightning Location Network (WWLLN) to count flashes from nearby storms
146 on the 4 days examined in this study. The CRLDN records lightning flashes within and near

147 Costa Rica with an efficiency that decreases with distance from the country. The network
148 consists of five IMPACT (Improved Performance from Combined Technology) sensors, similar
149 to those used in the U.S. NLDN [Cummins *et al.*, 1998] distributed throughout Costa Rica.
150 During TC⁴, the WWLLN consisted of a network of ~25 detectors distributed throughout the
151 world [Rodger *et al.*, 2006]. No complete global observations of the spatial variability of the
152 detection efficiency of WWLLN are available, although the efficiency has been increasing in
153 recent years as the network grows [Rodger *et al.*, 2008]. The WWLLN is 30–40% more efficient
154 at detecting flashes with peak currents above 40 kA, which is significantly higher than that of
155 typical CG flashes. There is also some indication that the detection efficiency is greater over
156 ocean than over land in the TC⁴ region [Lay *et al.*, 2009]. Both detector networks respond
157 primarily to CG flashes and to a smaller percentage of IC flashes. To obtain the total (IC + CG)
158 flash rate, it was necessary to scale the ground-based counts using a reference detector that
159 efficiently recorded both types of flashes. The reference used was data from the LIS instrument
160 on the Tropical Rainfall Measuring Mission (TRMM) [Boccippio *et al.*, 2002] satellite, recorded
161 during all overpasses of Costa Rica and surrounding areas during July and August 2007.

162

163 **2.2 OMI NO₂ data**

164

165 The OMI instrument is onboard the Aura satellite, which was launched July 2004 [Levelt *et al.*,
166 2006]. In addition to providing daily global measurements of ozone, OMI records other
167 important trace gases—notably NO₂. Because NO and NO₂ exist in photochemical equilibrium,
168 their sum, NO_x, is the quantity of interest. Due to differences in its absorption spectrum, NO is

169 not readily detectable from space, and the total NO_x amount must be inferred from
170 photochemical models.

171

172 The standard NO₂ product from OMI has been described by *Bucsela et al.* [2006, 2008] and
173 *Celarier* [http://toms.gsfc.nasa.gov/omi/no2/OMNO2_readme.pdf]. Backscattered radiation in
174 the form of spectral data from 60 pixels across the satellite track is imaged onto a CCD array, at
175 a spatial resolution of 13 × 24 km² at nadir. The spectrum at each pixel is fitted with an NO₂
176 absorption cross section to determine the total NO₂ slant column amount. In the OMNO2
177 product, the slant columns are also corrected for an instrumental artifact—the “cross-track
178 anomaly”—with a procedure that cross-track averages data from 15 consecutive orbits between
179 ±55° latitude. The cross-track anomaly correction is computed as an orbital constant at each of
180 the 60 cross-track positions. An air mass factor (AMF), defined as the ratio of a slant column
181 amount to the corresponding vertical column amount, is computed for a stratospheric NO₂ profile
182 and divided into the slant column to give an “initial” vertical column amount. The stratospheric
183 column amount is estimated from the global distribution of initial columns by masking polluted
184 regions and interpolating the remaining field in narrow latitude zones using planetary wave-2
185 functions. The tropospheric NO₂ vertical column—defined as positive—is computed from the
186 initial and stratospheric amounts and a tropospheric AMF.

187

188 For this study, we have developed a different method to estimate tropospheric NO₂ in the regions
189 affected by lightning (items 1–6 below). Some of the modifications in our approach (items 1–3
190 and 6) anticipate changes planned for the updated OMNO2 standard product data release due in
191 2010.

- 192 (1) Optimize the cross-track anomaly correction for tropical measurements
- 193 (2) Apply a correction to the stratospheric field to account for tropospheric contamination
- 194 (3) Compute tropospheric NO₂ slant column and allow positive and negative values.
- 195 (4) Use observed *in-situ* NO₂ profiles to get AMFs appropriate for convective outflow.
- 196 (5) Subtract background (non-lightning NO₂) derived from OMI data.
- 197 (6) Improve error estimates.

198 These are discussed further in Section 3.

199

200 **3. Analysis**

201

202 In this section we describe our approach for estimating the LNO_x signal from the OMI data. Data
203 from 4 days—July 17, 21, and 31 and August 5, 2007—were selected from the DC-8 flight days
204 during TC⁴ for analysis in this study; they are based on the combination of convective activity
205 within 12 hr of OMI overpass, as well as a detectable signal in the OMI NO₂ field near the
206 storms. The lightning signal was too weak to be detectable by OMI in the regions of two
207 additional convective systems sampled by the DC-8 (July 24 and August 8). Some of the
208 analysis also relies on aircraft measurements of *in situ* NO₂ from the DC-8. We also discuss use
209 of the lightning data from ground networks of detectors to obtain total flash estimates for each of
210 the regions studied.

211

212

213 **3.1 OMI NO₂ and LNO_x**

214

215 The LNO_x signal near convection is extracted from the OMNO2 data. The procedure involves
216 removal of the stratospheric and background-tropospheric components of the OMI slant columns
217 to yield a lightning-generated NO₂ (LNO₂) slant column. The slant column is divided by an AMF
218 representative of an LNO_x profile to yield the LNO_x vertical column, V_L, which is computed as
219 follows:

220
$$V_L = [S - V_{S'} \cdot A_S - V_{iBG} \cdot A_{iBG}] / A_{iL} \quad (1)$$

221 where

222 S is the OMNO2 slant column from the spectral fit (corrected for cross-track anomaly)

223 V_{S'} is the corrected stratospheric vertical column amount

224 A_S is the AMF for a stratospheric NO₂ vertical profile

225 V_{iBG} is the local tropospheric background NO₂ (non-lightning) from OMI data averaged over
226 days without significant convective activity

227 A_{iBG} is the local tropospheric background AMF (to ground) from OMNO2.

228 A_{iL} is a factor that converts the LNO₂ slant column to an LNO_x vertical column

229 In Equation (1) and subsequent equations, variables labeled V and S have units of column
230 density (e.g. molecules cm⁻²), and the air mass factors (A_S, A_{iBG}, and A_{iL} in Eq. 1) are unitless.
231 The quantity in brackets — the LNO₂ slant column — may have positive and negative values.

232

233 The slant columns obtained from the OMI spectral fit are corrected for the cross-track anomaly
234 during level-1 to level-2 processing. In this study, we have used a procedure different from that
235 applied in the OMNO2 standard product. Here the data that determine the anomaly are restricted
236 to tropical latitudes between $\pm 30^\circ$ (rather than the $\pm 55^\circ$ in OMNO2) and are based on the current
237 orbit, plus 2 adjacent orbits (rather than 15 adjacent orbits). This approach provides sufficient
238 statistics for accurately characterizing the anomaly function, while allowing for variation in the
239 anomaly function during each day and avoiding contamination from polluted regions at middle
240 latitudes.

241
242 The second term in Equation (1) is the corrected stratospheric slant column, which appears as the
243 product $V_S' \cdot A_S$, where the stratospheric AMF, A_S , is primarily a function of viewing geometry.
244 The corrected stratospheric field V_S' is given by

$$245 \quad V_S' = V_S - V_{tc} \cdot \bar{A}_t / \bar{A}_s, \quad (2)$$

246 where V_S is the “unpolluted” (essentially stratospheric) field from the wave-2 analysis in the
247 OMNO2 algorithm. This field is based on OMI data from “clean” regions defined by the
248 algorithm’s pollution mask. *Martin et al.* [2002] use a related approach in correcting data from
249 the central Pacific. The mask identifies areas that have annual mean tropospheric column
250 amounts less than $0.5 \times 10^{15} \text{ cm}^{-2}$, as estimated from the GEOS-Chem model [*Bey et al.*, 2001].
251 The stratospheric field is constructed from data in these relatively unpolluted areas. However, the
252 small amounts of tropospheric NO_2 in these regions can introduce a significant bias in the V_S ,
253 that can mask small amounts of tropospheric NO_2 (e.g., from lightning). We have corrected this
254 in the present study by subtracting zonal mean (within 9° -wide latitude bands) monthly
255 tropospheric column based on the NASA GMI chemical transport model [*Duncan et al.*, 2007].

256 V_{tc} is the mean GMI model tropospheric column in the “clean” regions around the zonal band.
257 Note that V_{tc} is distinct from V_{tBG} in Equation (1), which is derived from OMI data in the areas
258 of the TC⁴ study near Costa Rica. The factor \bar{A}_t/\bar{A}_s is the ratio of the mean tropospheric to
259 stratospheric AMF in the same regions used to estimate V_{tc} . We use a mean value of 0.7 for this
260 ratio. The resulting V_S' is an approximation of the true stratospheric component of the unpolluted
261 field measured by OMI. The difference between V_S and V_S' ranges from 0.04×10^{15} to $0.13 \times$
262 10^{15} cm^{-2} (~2–5%) and has a relatively large uncertainty, as described in Section 5.

263

264 The local tropospheric background is the third term in Equation (1). It is a slant column amount
265 equal to the product of the tropospheric vertical column, V_{tBG} , and the tropospheric background
266 AMF, A_{tBG} . Treating the background slant column in this manner neglects potential modification
267 of the background NO₂ profile due to local meteorological effects, but is a good approximation
268 for the small background amounts over tropical oceans [Beirle *et al.*, 2009]. Note that the AMF,
269 A_{tBG} , is computed from the complete NO₂ profile (tropopause to ground) in the presence of
270 clouds. Thus it implicitly accounts for clouds' effects on the *visibility* of background NO₂ from
271 OMI.

272

273 The tropospheric background in the vicinity of the TC⁴ study (Central America and surrounding
274 areas) was obtained from the average of 5 days of OMI data during July and August 2007,
275 selected on the basis of minimal convective activity. The small number of available days
276 reflected the fact that convection is a near-daily occurrence during the rainy season in this region.
277 The data were further screened using a maximum OMI cloud fraction threshold of 10%. Only
278 data from 2007 – the year of TC⁴ – were used in the analysis to minimize any effects from long-

279 term changes in tropospheric NO₂ or changes in OMI. For each pixel, the background was
 280 computed by subtracting the corrected OMI stratospheric amounts (Equation 2) from the slant
 281 columns and dividing by the tropospheric AMF, A_{tBG}. Both negative and positive values of the
 282 background were binned on a 2 x 2.5 deg² geographic grid. In spite of the strict pixel selection
 283 criteria, good statistics were obtained, with approximately 100 to 1000 pixels averaged per grid
 284 cell. We discuss alternative methods of estimating the tropospheric background in Section 5.

285

286 A_{tBG} is computed in the operational OMI algorithm using model NO₂ profiles and viewing
 287 geometry, and albedo and cloud information from the OMI data product for each measurement
 288 (OMI pixel). The expression is given by *Bucsela et al.* [2006] is modified as an integral over
 289 pressure, i.e.:

$$290 \quad A_{tBG} = \int \frac{dp}{p} \cdot r_{BG}(p) \cdot a(p) \cdot \beta(p) \quad (3)$$

291 Here the three unitless quantities in the integrand are defined as follows: $r_{BG}(p)$ is the
 292 normalized background NO₂ mixing-ratio profile, $a(p)$ is the atmospheric scattering weight (a
 293 function of viewing geometry, albedo, surface pressure, cloud pressure, and cloud height) and
 294 $\beta(p)$ is a temperature correction factor to adjust for the decrease in amplitude of the NO₂
 295 absorption cross section with temperature. Its value for temperatures in the troposphere and
 296 stratosphere is within 20% of unity. Temperatures are climatological geographically gridded (2 x
 297 5 deg²) monthly means from the National Centers of Environmental Prediction (NCEP). The
 298 temperature dependence is approximated as

$$299 \quad \beta(p) = 1 - 0.003 \cdot [T(p) - 220] \quad (4)$$

300 where $T(p)$ is the temperature (K), and the coefficient 0.003 K^{-1} accounts for the temperature
 301 variation in cross-section amplitude [Boersma *et al.*, 2001; Bucsela *et al.*, 2006]. The factor A_{IL}
 302 in the denominator of Equation (1), which may be thought of as the “LNO_x AMF”, is computed,
 303 following Beirle *et al.* [2009], as

$$304 \quad A_{\text{IL}} = \int \frac{dp}{p} \cdot \tau_{\text{LNO}_2}(p) \cdot a(p) \cdot \beta(p) / \gamma(p) \quad (5)$$

305 In Equation (5), $\gamma(p)$ is the photolysis ratio, $[\text{NO}_x]/[\text{NO}_2]$. The ratio depends on local chemistry
 306 and photolysis and thus varies with pressure, temperature, ozone concentration, and the amount
 307 of direct and scattered sunlight available. In this study, we use a simplified parameterization of
 308 $\gamma(p)$ based on three profiles of this quantity. These were obtained from the GMI model grid cells
 309 in the TC⁴ region; they represent maximum, mean, and minimum values for 1800 Universal
 310 Time Coordinated (UTC; near the OMI overpass time) in layers in the typical cloud outflow
 311 zone (500 to 100 hPa). The maximum γ ratio is used for regions above bright clouds, and the
 312 mean ratios are used within clouds, down to 100 hPa below cloud tops. The minimum γ ratios
 313 are used in all other regions, including clear areas.

314

315 The $\gamma(p)$ profiles are shown along with typical $a(p)$ and $\beta(p)$ profiles in Figure 2. The shapes of
 316 the profiles a and β show that radiative transfer effects enhance the sensitivity of the OMI slant
 317 column to NO₂ at higher altitudes (above ~600 hPa), where the majority of LNO₂ exists.
 318 However, this NO₂ represents only a small fraction of the lightning-generated NO_x, given that
 319 the γ profiles have values generally greater than 2 at these pressure levels.

320

321 We used a single composite NO₂ lightning profile, $r_{\text{LNO}_2}(p)$, in the computation. We assembled
322 it from the four TC⁴ DC-8 aircraft profiles containing the highest amounts of NO₂ above the 750
323 hPa level—the levels most influenced by lightning-generated NO_x. The profiles were binned
324 using median mixing ratios on a fixed pressure grid, similar to the approach used by *Bucsela et*
325 *al.* [2008]. Several of the profiles used for the composite, mostly measured near the airport,
326 contained significant amounts of pollution below 750 hPa. Therefore, we extrapolated the mixing
327 ratio of the composite profile at 750 hPa (~38 ppt) to ground. Because none of the four profiles
328 contained sufficient data above 300 hPa, we used three additional profiles from thunderstorm
329 anvil flights for the composite at these high altitudes. A background profile was assembled from
330 the DC-8 flights that contained the smallest NO₂ mixing ratios. This profile was subtracted from
331 the lightning composite. The resultant LNO₂ profile is shown along with the background in
332 Figure 2. The LNO₂ profile is qualitatively consistent with the LNO₂ profiles summarized by *Ott*
333 *et al.* [2009] from the Cirrus Regional Study of Tropical Anvils and Cirrus Layers-Florida Area
334 Cirrus Experiment (CRYSTAL-FACE), the European Lightning Nitrogen Oxides Project
335 (EULINOX), and the Stratosphere-Troposphere Experiments: Radiation, Aerosols & Ozone
336 (STERAO) campaigns, showing maxima between 4 and 10 km. The negligible amounts of NO₂
337 below 600 hPa in the LNO₂ profile are also consistent with the modeling studies of *Tie et al.*
338 [2001, 2002], who showed that the short lifetime of NO_x in the lower troposphere minimizes any
339 lightning enhancements in that region. Uncertainties associated with the LNO₂ profile shape are
340 discussed in Section 5.

341

342 A perimeter, constructed on a 1°-longitude x 1°-latitude grid defines the estimated region
343 influenced by lightning NO_x for the day in question. The regions were selected on the basis of

344 the location of recent (within the past 12 hr) convection, the mean upper-tropospheric wind
345 fields, and examination of the OMI NO₂ field. The regions were designed to minimize potential
346 effects by nearby convective systems. However, such effects remain a possible source of
347 contamination and represent a significant uncertainty in each of the case studies, except the July
348 17 case.

349

350 The value of V_L was obtained from Equation (1) for pixels having centers within the perimeter,
351 and a weighted sum was computed. Weights were based on the approximate area of overlap for
352 the pixel with the region. The total number of moles LNO₂ in region is the average V_L , times the
353 area of the region, divided by Avagadro's number.

354

355 **3.2 Flash counts**

356

357 Scaling factors to correct for inefficiencies in the CRLDN and WWLLN detectors (see Section
358 2.1) were computed using several weeks of data from the LIS satellite instrument. This approach
359 was necessary since the LIS only observes a given point on the Earth for ~90 seconds during an
360 overpass and therefore could not provide measurements over entire lifetimes of the individual
361 storms examined here. The CRLDN and concurrent LIS data from overpasses in the vicinity of
362 Costa Rica during July and August 2007 were binned in concentric rings in radius steps of 200
363 km around the middle of Costa Rica. Only CRLDN flashes that occurred within the LIS field of
364 view were considered in this analysis. From these data, we derived detection fractions for total

365 flashes (CG + IC) in each ring. The scaling factor for CRLDN data, ϵ_C (the inverse of detection
366 fraction) is:

$$367 \quad \epsilon_C = \langle F_{\text{LIS}} / F_{\text{CRLDN}} \rangle \quad (6)$$

368 where F_{LIS} are the LIS satellite flash counts, F_{CRLDN} are the raw CRLDN counts, and $\langle \rangle$ refers to
369 averaging in a given ring over the 2 months. Before their use in this calculation, we adjusted the
370 LIS flash counts for the detection efficiency of this instrument on the basis of values provided by
371 *Boccippio et al.* [2002] (e.g., 69% at local noon and 88% at night). Values of ϵ_C determined for
372 this period were 1.40 in the 0–200 km radius ring, 2.80 in the 200–400 km radius ring, and 9.17
373 in the 400–600 km ring. Beyond 600 km, the CRLDN data become too uncertain to use in LNO_x
374 analyses. We used ϵ_C to obtain adjusted CRLDN counts, F'_{CRLDN} , for the July 31 storm, which
375 was located near the CRLDN network, and took this value to be the best estimate of total number
376 of flashes for that storm; that is,

$$377 \quad F_{\text{Total}} = F'_{\text{CRLDN}} = F_{\text{CRLDN}} \cdot \epsilon_C \quad (7)$$

378 We also estimated the detection fraction of the WWLLN network in the TC⁴ region. The flash
379 counts from the CRLDN (adjusted using ϵ_C) and WWLLN for six storms during the TC⁴ period
380 in the vicinity of Costa Rica were compared to obtain a second scaling factor ϵ_W . The factor is

$$381 \quad \epsilon_W = \langle F'_{\text{CRLDN}} / F_{\text{WWLLN}} \rangle \quad (8)$$

382 where F_{WWLLN} is the WWLLN flash count. In this case, no information on the spatial variability
383 of the WWLLN is available, because the averaging was done over six storms, all of which were
384 near Costa Rica. We obtained a mean value $\epsilon_W = 4.57$ with an error of $\pm 36\%$. This factor was

385 used to compute the total flash counts on July 17 and 21 and August 5, when storms were
386 relatively far from the CRLDN network; that is,

$$387 \quad F_{\text{Total}} = F_{\text{WWLLN}} \cdot \epsilon_{\text{W}} \quad (9)$$

388 Dividing the estimated total flash counts into the moles of LNO_x in the corresponding region
389 gives the estimated number of mole per flash.

390

391 **4. Results**

392

393 We obtained measurable OMI NO₂ signals near convection on 4 of the 6 days during the TC⁴
394 experiment on which the aircraft sampled thunderstorm anvils. All four convective systems
395 analyzed are located over the ocean. Therefore, convective transport of surface emissions of NO_x
396 into the anvils of these systems was assumed to be negligible. By comparing the OMI NO₂ field
397 with the cloud field and lightning measurements, and estimating the effects of transport due to
398 mid-tropospheric wind fields, we identified regions of possible LNO_x enhancement. The OMI
399 effective geometrical cloud fraction on those days is shown in Figure 3, and the LNO_x fields over
400 the same areas, computed as outlined in Section 3, are shown in Figure 4.

401

402 Most of the regions in Figure 3 are partly cloudy, and we estimate values of A_{TL}, between 0.2 and
403 0.8, with most values in the range of 0.4 to 0.5. These factors compare well with the factors
404 estimated in the model study of *Beirle et al* [2009] (referred to as “sensitivity factors” in that
405 study), in spite of the simpler fixed LNO₂ profile and approximation of opaque Lambertian
406 clouds used in the present study. *Ott et al.* [2009] estimated the LNO₂ signal that might be seen

407 in satellite measurements over convective clouds, based on visible-near-UV penetration of
408 radiation to a depth of 400–600 hPa. Their calculations suggested LNO₂ tropospheric vertical
409 columns of $0.1 - 2.0 \times 10^{15} \text{ cm}^{-2}$ should be detectable over active convection. In the present
410 study, the mean LNO₂ column in each of the regions analyzed ranged from $0.1-0.3 \times 10^{15} \text{ cm}^{-2}$.

411

412 Table 1 summarizes information about the regions studied on the 4 days. Shown are the areas of
413 the polygons, the mean anvil-level wind velocities from NCEP reanalysis, the moles of LNO_x,
414 flash counts, and the resultant LNO_x production rates. Derivation of the uncertainty estimates is
415 given in Section 5.

416

417 LNO_x production per flash was found to be somewhat lower—87 to 135 mol/flash—in the first
418 two cases (July 17 and 21, respectively) and higher—246 and 227 mol/flash—in the latter two
419 cases (July 31 and August 5, respectively), with uncertainties in each case on the order of 100%.

420 We note that the first two cases had relatively light anvil-level (300 hPa) wind speeds (2–6 m/s)
421 and that the latter two cases had stronger winds at anvil level (8–13 m/s). These results are
422 suggestive of agreement with the results of *Huntrieser et al.* [2008], who found greater LNO_x
423 production in storms with greater vertical wind shear. The *Huntrieser et al.* analysis suggests that
424 longer flash length occurs with stronger upper level winds and that the greater length is
425 responsible for greater production per flash. *Huntrieser et al.* [2009] suggest that even within the
426 tropics, substantial variability in production per flash can occur, and may also be related to flash
427 length and associated wind profiles.

428

429 **5. Discussion**

430

431 The moles per flash estimates in this study are associated with large uncertainties. In this section
432 we examine the sources of uncertainty in the production estimates and employ comparisons with
433 independent aircraft data obtained during TC⁴. We also discuss the current results in the context
434 of those from previous studies.

435

436 **5.1 Uncertainties**

437

438 The small magnitude and spatial extent of LNO₂ enhancements make precise measurements
439 difficult, as reflected in the large uncertainties in moles per flash obtained this study. We
440 distinguish between two types of errors: (1) those related to pixel-scale measurement variability,
441 which we treat as statistical errors, and (2) systematic errors associated with larger scale
442 variability. The latter are the largest component of the overall uncertainties in the moles per flash
443 numbers. In this section we discuss the estimation of both types of errors and their propagation.
444 To identify all sources of uncertainty, Equation (1) can be rewritten explicitly as follows:

445
$$V_L = \sum_i w_i \cdot [S_i - (V_{si} - V_{tc\ i} \cdot \bar{A}_t / \bar{A}_s + \delta V_s) \cdot A_{si} - (V_{tbg\ i} + \delta V_t) \cdot A_{tbg\ i}] / A_{tLi} \quad (10)$$

446 The summation in Equation (10) is over all pixels, *i*, in the region of interest (bounded by the
447 perimeters in Figures 3). As in Equation (1) all quantities are unitless except the V and S terms,
448 which have units of column density. The individual pixel errors are computed independently for

449 each term subscripted with i and are assumed, for simplicity, to be uncorrelated. Here w_i is the
450 weighting factors based on the pixel area. The errors in the slant columns, S_i , were derived in the
451 spectral fit and found to be consistent with the pixel-to-pixel spatial variability of slant columns.
452 The terms δV_s and δV_t are modifications to Equation (1) and identify sources of systematic error,
453 relatively independent of individual pixels. They stand for potential biases in the derived
454 stratosphere and troposphere, respectively. These terms, described below, have mean values of
455 zero, but are given fixed finite uncertainties, independent of pixel area.

456

457 The random error at each pixel results from uncertainties in several terms (each subscripted with
458 i) in Equation (10). The small-scale uncertainty in the OMI stratospheric column, V_{si} , is
459 conservatively estimated to be $0.2 \times 10^{15} \text{ cm}^{-2}$ [Boersma *et al.*, 2004; Bucsela *et al.*, 2006]. The
460 model column amount $V_{tc i}$ is assigned a random error of 40%, based on a set of clean profiles
461 measured during TC⁴ and consistent with GMI model variability in the region of the TC⁴ study
462 (see Figure 5). The same 40% random error is assumed for $V_{tbg i}$, also from GMI. Errors in the
463 AMFs depend on estimates of cloud parameters, surface albedos, and a priori profile shape
464 variability. They are computed using an off-line algorithm [Wenig *et al.*, 2008] that improves on
465 the OMNO2 collection 3 uncertainties. The largest sources of error in each AMF are the clouds,
466 which can shield or enhance the visibility of NO₂. For each pixel, the errors in cloud fraction and
467 cloud pressure are propagated into the overall AMF error, based on radiative transfer and the
468 uncertainty in the amount of NO₂ masked by the cloud. This uncertainty is large (on the order of
469 100%) in the case of convective clouds, since they shield most of the troposphere and can
470 significantly modify the NO₂ distribution beneath them. Clouds also affect the NO_x photolysis
471 ratio. The uncertainty in γ is roughly 50% in the upper troposphere, decreasing to ~10% near the

472 surface. Since most of the LNO₂ is observed in the upper troposphere, we conservatively assign
473 an uncertainty of 50% to the photolysis ratios, and this uncertainty leads to an additional 50%
474 error in each value of A_{Li}.

475

476 The uncertainty in δV_s is a large source of error. We compute this error from an estimate of the
477 potential error introduced by the wave-2 method used to derive the stratosphere in the OMI NO₂
478 algorithm. Other NO₂ satellite retrieval algorithms employ the Pacific Reference Sector (PRS)
479 method [e.g., *Martin et al.*, 2002; *Richter and Burrows*, 2002], which assumes a constant
480 stratospheric amount at each latitude based on data over the central Pacific Ocean at that latitude.
481 The DOMINO algorithm used to process OMI NO₂ data for the Dutch near-real time product
482 assimilates OMI slant columns into the TM4 model, weighting the data according to model
483 estimates of tropospheric contamination [*Boersma et al.*, 2007]. Our comparisons of these
484 models show that stratospheric estimates at middle and high latitudes can differ by as much as
485 0.5 to $1.0 \times 10^{15} \text{ cm}^{-2}$. At tropical latitudes, the differences tend to be smaller—on the order of
486 0.1 to $0.2 \times 10^{15} \text{ cm}^{-2}$. Stratospheric fields from both methods for the July 21 case are shown in
487 Figure 5. For the 4 days examined in this study, the PRS and wave-2 methods were tested and
488 gave mean stratospheric values that varied by 0.01 to $0.12 \times 10^{15} \text{ cm}^{-2}$, with an average
489 difference of $0.07 \times 10^{15} \text{ cm}^{-2}$. For the model correction due to contamination of the stratosphere
490 by small amounts of tropospheric NO₂, we estimate an uncertainty of $\sim 0.05 \times 10^{15} \text{ cm}^{-2}$.
491 Combining these values we adopt a conservative estimate of the potential systematic error in the
492 tropical stratosphere of $0.1 \times 10^{15} \text{ cm}^{-2}$, or about 4%.

493

494 The OMI tropospheric background columns are shown in Figure 6. The error in the background
495 is another significant source of uncertainty in the analysis. In this study, the standard deviation of
496 pixel variation in each $2 \times 2.5 \text{ deg}^2$ grid cell is used to represent the statistical (pixel-to-pixel)
497 uncertainty in the background, and the standard error of the mean is taken as the systematic
498 uncertainty. This estimate of the systematic uncertainty assumes that the approach used in this
499 study for computing the background – i.e. from OMI data on days without convection – is
500 reasonable. Here we briefly examine several alternative approaches considered in this study for
501 obtaining this background, including the use of *in situ* data and GMI model calculations to
502 estimate the background. In one approach, a composite profile was constructed from DC-8
503 measured profiles that showed relatively small amounts of NO_2 above 600 hPa, where most
504 LNO_2 is typically found. The integrated tropospheric column for this profile was $0.67 \pm 0.29 \times$
505 10^{15} cm^{-2} , which is generally consistent with the gridded columns from OMI (Figure 6).
506 However, use of this fixed value does not account for spatial gradients evident in the
507 tropospheric NO_2 field. We also investigated use of model background fields computed from
508 GMI runs in which the lightning source was turned off. Such backgrounds were less than half of
509 those derived from OMI. Since they do not account for NO_2 from lightning flashes not included
510 in the flash-count estimates (e.g. from storms on previous days), they are unlikely to accurately
511 represent the background field. Moreover, any model calculations or *in situ* measurements are
512 likely to contain unknown biases relative to OMI data. Subtracting a background computed in
513 the same way as the total NO_2 column measurements – i.e. from OMI data – helps to minimize
514 such biases.

515

516 Results of this study were found to be relatively insensitive to the background NO_2 or LNO_2
517 profile shapes. In the case of the LNO_2 profile, subtraction of the background component from
518 the composite, as described in Section 3.1, affected the value of A_{tLi} at any given pixel by only
519 about 5%. This finding is reasonable, since the subtraction only slightly affects the scaling
520 factors (A_{tLi}) used to convert the LNO_2 slant columns to LNO_x vertical columns (i.e., it does not
521 remove the background column V_{tBG}). Most of the NO_2 in the lightning profile exists above 700
522 hPa. Effects of profile shape changes on A_{tLi} in this region are mainly due to the gradient in
523 photolysis ratio as a function of pressure level (Figure 2b). We examined the effect of replacing
524 the LNO_2 profile in Figure 2a with a profile composed only of the DC-8 anvil data that has
525 negligible NO_2 below 300 hPa. The result was a ~20% change in the value of A_{tLi} . We treat this
526 change as a systematic uncertainty in the results and include it in the error calculation, although
527 its effect on the total error budget is negligible.

528

529 An additional systematic source of error in the computed moles of LNO_x results from the
530 selection of the geographic area of interest. One component is imprecise knowledge of the wind
531 fields, which makes the position of the regions' centers uncertain. We did not attempt detailed
532 trajectory analysis of the convective outflow in this study, given the difficulty in estimating
533 convective perturbations to the analyzed ambient winds during the few hours between storm
534 development and OMI overpass. Therefore, we have used the mean wind speed and direction in
535 the vicinity of the storm and immediately downwind from the 300 hPa NCEP analysis and the
536 number of hours between storm development and the OMI overpass to estimate the region
537 affected by the outflow. This region generally corresponded to the location of enhancements in
538 LNO_x downwind of the storm. Assuming the 10–15% variability of the analyzed winds from

539 NCEP and lightning occurring throughout a 12-hr period preceding the OMI overpass, we
540 estimate the transport distance along the mean wind vectors to have an error less than or equal to
541 $\pm 0.3^\circ$ of latitude. Adjusting the geographic positions of the regions by this amount along the
542 wind vectors allows us to estimate the sensitivity of the LNO_x calculation to the wind field.

543

544 Another uncertainty in the region selection is the size of each area. We estimate that storm-
545 outflow regions can be identified in the OMI NO₂ field to a resolution of approximately 1° and
546 have drawn the perimeters in each case accordingly (see Figure 4). From this we obtain the
547 approximate uncertainty in the enclosed areas following the approach of *Ghilani* [2000] and
548 uniformly expand and shrink the regions by the same amount to determine the effect on the
549 derived moles of LNO_x.

550

551 The combined effects of the uncertainties in the regions' areas and positions lead to uncertainties
552 in the computed number of moles on the order of 20–30%. The areal uncertainty makes the
553 larger contribution. Further uncertainties exist because of the possible contamination due to
554 LNO_x from neighboring convective systems, for which lightning counts were not available.
555 Although the region perimeters were drawn to minimize such contamination, nearby storms
556 potentially influenced the results for each day, except July 17. Because we did not estimate the
557 magnitude of this influence in this study, the moles LNO_x and moles per flash estimates we
558 obtained must be considered upper limits, and the uncertainties may be larger than those
559 indicated here.

560

561 The final source of error is uncertainty in the number of flashes that contribute to the LNO_x
562 enhancements. The flash-count error depends on the method used to obtain the counts. For the
563 July 31 case, the adjusted counts were obtained from the CRLDN and have an error of 10–20%.
564 In the other cases, the adjustment factor $\epsilon_w = 4.57$ used to scale the WWLLN has an uncertainty
565 of ± 1.66 , or 36%.

566

567 Table 2a summarizes the error sources in the calculation of LNO_x, and Table 2b shows their
568 contributions along with those of flash uncertainties to the overall error in each of the four cases.
569 As seen in Table 2a, the largest sources of error are the systematic error in the stratosphere and
570 tropospheric background over the region. In the table, we combine these errors with the
571 systematic profile-shape uncertainty, which makes a smaller contribution. The uncertainty in the
572 flash count rate is shown in Table 2b. The random variations can be large for a given pixel, but
573 are a small part of the error budget due to the statistical averaging of a large number of OMI
574 pixels. Although our calculation of the relative error is largest for the July 17 case, this case was
575 less affected by neighboring convection (which is not explicitly accounted for here) than by the
576 other days; consequently, the actual uncertainties on those days may be larger than shown.

577

578 **5.2 Additional analysis considerations**

579

580 As outlined in Section 2.2, the procedure we use to extract the LNO_x signal from OMI data is a
581 customized retrieval algorithm optimized for the TC⁴ study. However it also includes
582 modifications to the OMNO₂ data – including improved error estimates – that are being

583 considered in a future release of this data product. Modifications (1) – (3) were found to alter the
584 production-rate values obtained in this study by up to 40% when combined, and by a factor of
585 two or more if the changes are implemented separately. The smaller discrepancy for the
586 combined modifications is due to the fact that some changes – e.g. the stratospheric correction –
587 increases the LNO₂ signal, while others – e.g. the inclusion of negative tropospheric values – act
588 to decrease the mean signal. These findings highlight the importance of careful analysis as well
589 as the general difficulty in determining lightning NO₂ enhancements from satellite observations
590 of individual storms.

591
592 Additional independent aircraft data are available for comparison with the satellite
593 measurements. We examined the NO_x enhancement over background due to lightning as
594 computed from OMI and compared results with estimates from the *in situ* DC-8 observations
595 within and near the observed convective systems. For times when either NO or NO₂ was missing
596 from the aircraft data set, we estimated it using a photostationary state calculation. Table 3
597 presents the means and standard deviations of the in-cloud and nearby clear-air aircraft
598 observations, the OMI LNO_x column amounts, and the column amounts of NO_x in the
599 tropospheric background as estimated from OMI tropospheric NO₂ on non-convective days. In
600 the table, OMI LNO_x column represents the signal above the background – ie not the total NO_x
601 column. The aircraft enhancements are computed as the ratio of the in-cloud measurements to
602 the clear-air measurements. Although it is likely that most of the NO₂ profiles from DC-8
603 contained at least some lightning-generated NO₂ in the tropospheric column, the anvil-level
604 clear-air measurements used for these ratios were carefully screened for LNO₂ contamination.
605 The LNO_x enhancement in the broader-scale convective outflow (as seen by OMI) should be less

606 than but roughly proportional to the in-anvil enhancement (as measured by the DC-8). The DC-8
607 data show enhancement factors due to lightning of between 1.74 and 2.35. Enhancements in the
608 OMI LNO_x column are calculated as the sum of OMI + background, divided by background. The
609 OMI enhancement factors range from 1.2 to 1.4. These values are somewhat smaller than the
610 DC-8 factors as might be expected, since the OMI ratios are derived from column rather than *in*
611 *situ* measurements. The OMI background columns, in particular, include significant NO_x in the
612 lower troposphere that was not included in the DC-8 calculation.

613

614 **5.3 Other studies of LNO_x production per flash**

615

616 The production efficiencies for LNO_x from the storms in this study range from ~100 to 250
617 mol/flash. This range is relatively modest given the wide range found in the literature and the
618 large uncertainties in the results. The mean value over the 4 cases of 174 mol/flash is lower than
619 the 360 mol/flash derived by *Ott et al.* [2007] in their analysis of a mid-latitude storm. However,
620 it is comparable to the production rates that *Huntreiser et al.* [2008] obtained in their study of
621 tropical and subtropical storms during the Brazilian Tropical Convection, Cirrus and Nitrogen
622 Oxides Experiment (TROCCINOX) experiment. Using total flash counts derived from LIS
623 measurements, *Huntreiser et al.* [2008] estimated production of 1–3 kg(N)/flash, which
624 corresponds to ~70–200 mol/flash. They hypothesized that the smaller production rates for the
625 lower latitude storms were related to disparities in production by flashes at different latitudes, as
626 we discuss below.

627

628 *Ott et al.* [2009] summarized analyses of five mid-latitude and subtropical storms simulated
629 using a 3-D cloud-scale model. The storms were observed during the STERAO, EULINOX, and
630 CRYSTAL-FACE field campaigns. They derived production efficiencies for CG flashes, based
631 on observations of the CG and IC flash rates and on comparisons of their model simulations with
632 aircraft observations of NO_x in the storms. They also compared their results to estimates of P_{CG}
633 from *Price et al.* [1997] and *Fehr et al.* [2004]. With the exception of the *Price et al.*'s [1997]
634 theoretical value of P_{IC}/P_{CG} = 0.1, most recent results indicate that IC and CG flashes produce
635 equal amounts of NO on average, in agreement with the recommendation of *Ridley et al.* [2005].
636 Therefore, for the purpose of comparing results of the present study with the P_{CG} and P_{IC}
637 estimates from *Ott et al.* [2009] and other studies, we adopt a value of unity for P_{IC}/P_{CG}. These
638 comparisons are shown in Figure 7 as a function of latitude and anvil-level wind speed. Although
639 there appears to be no universal relationship linking production per flash to latitude or anvil-level
640 wind speed, for a particular experiment larger production per flash values are associated with
641 stronger upper-level winds. We also note that lower (higher) production rates among the studies
642 were generally obtained for storms at lower (higher) latitudes.

643

644 The average number of moles per flash over the four cases from the present study of tropical
645 convection (174) is lower than the ~500 mol/flash average derived from the mid-latitude and
646 subtropical storms of the *Ott et al.* [2009] study. *Ott et al.* extrapolated the 500 mol/flash to
647 estimate global LNO_x production at 8.6 Tg (N) yr⁻¹, which is near the high end of the range of 2
648 to 8 Tg (N) yr⁻¹ from *Schumann and Huntrieser* [2007]. They suggest the high value may be due
649 to neglect of tropical storms in their study. The lower production rates of the present TC⁴ study
650 are consistent with the hypothesis that NO_x production per flash is typically lower in the tropics

651 than at higher latitudes. A possible reason for the latitudinal variation relates to the nature of
652 lightning flashes in storms at low and middle latitudes. In general, the LNO_x production rate for a
653 given flash depends on the intensity of the flash, the flash length, and the pressures at which the
654 flash occurs. Although a greater fraction of a CG flash occurs at higher pressure than an IC, this
655 effect may be counterbalanced, in mid-latitude storms by the longer IC flash lengths (*Ott et al.*,
656 2007; 2009), leading to near equal LNO_x production per flash for IC and CG flashes. *Huntreiser*
657 *et al.* [2008] hypothesize that flash lengths in mid-latitudes and subtropics are greater than flash
658 lengths in the tropics because of greater vertical wind shear at the higher latitudes—leading to
659 greater LNO_x production per flash outside of the tropics. Our results for the storms of July 17
660 and 21 showed production rates (averaged over IC and CG flashes) close to the low end of the
661 range from the TROCCINOX analysis of *Huntreiser et al.* [2008] and somewhat larger rates for
662 the storms of July 31 and August 5. Anvil-level winds were stronger in the 300 hPa NCEP
663 reanalysis fields for July 31 and August 5 than for July 17 and 21, suggesting possible longer
664 flash lengths in these cases, with greater LNO_x production per flash. It is also possible that
665 contamination from nearby convection (not included in the flash counts) may have contributed to
666 the larger LNO_x amounts on those days, but this may have also been the case for one of the days
667 with low LNO_x production rate (July 21).

668

669 **5.4 Flash footprints**

670

671 Further evidence for the effects of wind shear may be seen in the LIS data, which can be used to
672 obtain information on the extent of lightning flashes. The LIS sensor operates as a lightning

673 event detector on a charge coupled device (CCD). An event is defined as the occurrence of a
674 single CCD pixel exceeding the background threshold during a single frame. Because a single
675 pixel will almost never correspond to the exact cloud illumination area, a lightning discharge will
676 often illuminate more than one pixel during a single integration time. The result is two or more
677 events that are clustered in space and time (groups). A lightning flash may also correspond to
678 several related groups in a limited area [*Christian et al.*, 1994]. Integrating the area of all CCD
679 pixels involved in a flash provides the “footprint” of the flash [*Boccippio et al.*, 1998], which can
680 be interpreted as its horizontal extent.

681

682 LIS viewed only one of the four storms analyzed here (July 21). Figures 8a and 8b show,
683 respectively, the flash rate density and the event rate density of the July 21 case. It can be seen
684 that all convective cores of the cloud (orange tones in Figure 1b) produced flashes, at a rate up to
685 $7.46 \text{ flashes km}^{-2} \text{ s}^{-1}$ on the north cell. Although only a few flashes were detected in the center of
686 the storm, the event rate density shows that area illuminated by those flashes corresponds to a
687 fairly large extent of the convective cores, delineating the sum of flash footprints. The statistics
688 of individual flash footprints of the July 21 case is presented in Figure 8c, and is compared to the
689 statistics of all LIS flashes recorded throughout the tropics (35°S to 35°N) during the boreal
690 summer (June, July and August) of 2007 (Figure 8d). Note that the distribution for the July 21
691 storm north of Colombia is skewed toward smaller footprint sizes ($<556 \text{ km}^2$) compared with the
692 nearly perfect Gaussian distribution for 2007 boreal summer. Assuming that the LIS footprint
693 can be considered a proxy for flash length, this result suggests that there was a greater frequency
694 of short flashes for this storm than is typical for this latitude band. The small magnitude of the
695 LNO_x production per flash obtained from our analysis of OMI NO_2 data for this storm, combined

696 with the weak upper tropospheric wind speeds and the smaller LIS footprint, supports the
697 *Huntrieser et al.* [2008] hypothesis.

698

699 **6. Conclusions**

700

701 We have developed an algorithm to retrieve realistic LNO_x signals from OMI. Improvements
702 over the standard retrieval include a more exact treatment of the stratospheric NO₂ column and
703 an improved cross-track anomaly correction. To customize the retrieval for LNO_x, we have
704 removed background tropospheric NO₂ column amounts using the GMI model, and used an
705 AMF appropriate for a profile shape characteristic of convective outflow (based on TC⁴ aircraft
706 observations). The technique has been applied to four TC⁴ flight day convective events occurring
707 over the ocean offshore from Costa Rica, Panama, and Colombia. Combining these TC⁴ data
708 with flash observations, we estimate LNO_x production per flash for each of the selected cases.
709 Due to the small LNO_x signals in these cases, and the large uncertainties inherent in the analysis
710 – notably in the background stratospheric and tropospheric estimates –the uncertainties in the
711 retrieved LNO_x amounts are very large. However, results from our study are generally consistent
712 with previous estimates of lightning NO_x production rates. The findings indicate that LNO_x
713 production per flash was ~200–250 mol/flash for two cases with stronger upper level winds, and
714 near 100 mol/flash for two cases with weaker anvil-level transport, supporting the contention that
715 tropical LNO_x values may be lower than those found at higher latitudes. Flash footprint size
716 information from the LIS instrument suggests that for the storm with the smallest LNO_x
717 production per flash estimate the flash lengths were shorter than is typical. The enhancement due
718 to LNO_x above background levels determined using OMI NO₂ data is in agreement with the

719 enhancement seen in *in situ* anvil NO_x observations over background observations taken by the
720 DC-8 aircraft in TC⁴, thereby providing validation of the LNO_x retrieval method.

721

722 **Acknowledgements**

723

724 This research was supported by the NASA Aura Validation Program. Lightning data from the
725 Costa Rica Lightning Detection Network were provided by Instituto Costarricense de
726 Electricidad.

727

728 **References**

729

730 Beirle, S., N. Spichtinger, A. Stohl, K. L. Cummins, T. Turner, D. Boccippio, O. R. Cooper, M.
731 Wenig, M. Grzegorski, U. Platt, and T. Wagner, (2006), Estimating the NO_x produced by
732 lightning from GOME and NLDN data: A case study in the Gulf of Mexico, *Atmos.*
733 *Chem. Phys.*, *6*, 1075–1089.

734 Beirle, S., U. Platt, M. Wenig, and T. Wagner, (2004), NO_x production by lightning estimated
735 with GOME, *Adv. Space Res.*, *34*(4), 793–797.

736 Beirle, S., M. Salzmann, M. G. Lawrence, and T. Wagner, (2009), Sensitivity of satellite
737 observations for freshly produced lightning NO_x, *Atmos. Phys. Chem.*, *9*, 1077–1094.

738 Bey, I., D. J. Jacob, R. M. Yantosca, J. A. Logan, B. D. Field, A. M. Fiore, Q. Li, H. Y. Liu, L. J.
739 Mickley, and M. G. Schultz, (2001), Global modeling of tropospheric chemistry with

740 assimilated meteorology: Model description and evaluation, *J. Geophys. Res.*, *106*,
741 23073–23096.

742 Boccippio, D. J., W. J. Koshak, and R. J. Blakeslee, (2002), Performance assessment of the
743 Optical Transient Detector and Lightning Imaging Sensor. Part I: Predicted diurnal
744 variability, *J. Atmos. Oceanic Technol.*, *19*, 1318–1332.

745 Boccippio, D., K. Driscoll, J. Hall, and D. Buechler (1998), LIS/OTD Software Guide, Global
746 Hydrology and Climate Center, pp.142. Available on-line at
747 ftp://ghrc.nsstc.nasa.gov/pub/doc/lis/LISOTD_UserGuide.pdf

748 Boersma, K. F., E. J. Bucsela, E. J. Brinksma, J. F. Gleason, NO₂ (2001), *OMI-EOS Algorithm*
749 *Theoretical Basis Document: Trace Gas Algorithms: NO₂*, chap. 4, pp. 12–35, Royal
750 Netherlands Meteorological Institute, De Bilt, Netherlands.

751 Boersma, K. F., H. J. Eskes, and E. J. Brinksma, (2004), Error analysis for tropospheric NO₂
752 from space, *J. Geophys. Res.*, *109*, D04311, doi:10.1029/2003JD003962.

753 Boersma, K. F., H. J. Eskes, E. W. Meijer, and H. M. Kelder, (2005), Estimates of lightning NO_x
754 production from GOME satellite observations, *Atmos. Chem. Phys.*, *5*, 2311–2331.

755 Boersma, K. F., H. J. Eskes, J. P. Veefkind, E. J. Brinksma, R. J. van der A, M. Sneep, G.H.J.
756 van den Oord, P. F. Levelt, P. Stammes, J. F. Gleason, and E. J. Bucsela, (2007), Near-
757 real time retrieval of tropospheric NO₂ from OMI, *Atmos. Chem. Phys.*, *7*, 2103–2118.

758 Bond, D. W., S. Steiger, R. Zhang, X. Tie, and R. E. Orville, (2002), The importance of NO_x
759 production by lightning in the tropics, *Atmos. Env.*, *36*, 1509-1519.

760 Bucselá E., E. Celarier, M. Wenig, J. F. Gleason, P. Veefkind, K. F. Boersma, and E. Brinksma,
761 (2006), Algorithm for NO₂ vertical column retrieval from the Ozone Monitoring
762 Instrument, *IEEE Trans. Geosci. Remote Sensing*, 44, 1245–1258.

763 Bucselá, E. J., A. E. Perring, R. C. Cohen, K. F. Boersma, E. A. Celarier, J. F. Gleason, M. O.
764 Wenig, T. H. Bertram, P. J. Wooldridge, R. Dirksen, and J. P. Veefkind, (2008),
765 Comparison of tropospheric NO₂ from *in situ* aircraft measurements with near-real-time
766 and standard product data from OMI, *J. Geophys. Res.*, 113, D16S31,
767 doi:10.1029/2007JD008838.

768 Christian, H., R. Blakeslee, S. Goodman, and Douglas Mach (1994), Algorithm Theoretical
769 Basis Document (ATDB) for the Lightning Imaging Sensor (LIS), George C. Marshall
770 Space Flight Center, National Aeronautics and Space Administration. Available on-line
771 at http://eosps0.gsfc.nasa.gov/eos_homepage/for_scientists/atbd/docs/LIS/atbd-lis-01.pdf

772 Cummins, K. L., M. J. Murphy, E. A. Bardo, W. L. Hiscox, R. B. Pyle, and A. E. Pifer, (1998),
773 A combined TOA/MDF technology upgrade of the U.S. National Lightning Detection
774 Network, *J. Geophys. Res.*, 103, 9035–9044.

775 DeCaria, A. J., K. E. Pickering, G. L. Stenchikov, and L. E. Ott, (2005), Lightning-generated
776 NO_x and its impact on tropospheric ozone production: A three-dimensional modeling
777 study of a Stratosphere-Troposphere Experiment: Radiation, Aerosols and Ozone
778 (STERA0-A) thunderstorm, *J. Geophys. Res.*, 110, D14303, doi:10.1029/2004JD005556.

779 Duncan, B. N., S. E. Strahan, Y. Yoshida, S. D. Steenrod, and N. Livesey, (2007), Model study
780 of the cross-tropopause transport of biomass burning pollution, *Atmos. Chem. Phys.*, 7,
781 3713–3736.

782 Fehr, T., H. Höller, and H. Huntrieser, (2004), Model study on production and transport of
783 lightning-produced NO_x in a EULINOX supercell storm, *J. Geophys. Res.*, *109*, D09102,
784 doi:10.1029/2003JD003935.

785 Ghilani, C. D., (2000), Demystifying area uncertainty: More or less. *Survey. Land Inf. Syst.*,
786 *60*(3):177–182.

787 Huntrieser, H., U. Schumann, H. Schlager, H. Holler, A. Giez, H.-D. Betz, D. Brunner, C.
788 Forster, O. Pinto Jr, and R. Calheiros, (2008), Lightning activity in Brazilian
789 thunderstorms during TROCCINOX: Implications for NO_x production, *Atmos. Chem.*
790 *Phys.*, *8*, 921–953.

791 Huntrieser, H., H. Schlager, M. Lichtenstern, A. Roiger, P. Stock, A. Minikin, H. Hoeller, K.
792 Schmidt, H.-D. Betz, G. Allen, S. Viciani, A. Ulanovsky, F. Ravegnani, and D. Brunner,
793 (2009), NO_x production by lightning in Hector: First airborne measurements during
794 SCOUT-O3/ACTIVE, *Atmos. Chem. Phys. Discuss.*, *9*, 14361–14451.

795 Jaeglé, L., D. J. Jacob, Y. Wang, A. J. Weinheimer, B. A. Ridley, T. L. Campos, G. W. Sachse,
796 and D. E. Hagen, (1998), Sources and chemistry of NO in the upper troposphere over the
797 United States, *Geophys. Res. Lett.*, *25*, 1709–1712.

798 Lay, E. H., C. J. Rodger, R. H. Holzworth, A. R. Jacobson, D. M. Suszcynsky, J. N. Thomas, and
799 J. B. Brundell, (2009), World-wide Lightning Location Network: Improvements in global
800 detection efficiency and estimated stroke energy, Fourth Conference on the
801 Meteorological Applications of Lightning Data, American Meteorological Society,
802 Phoenix, AZ.

803 Levelt, P. F., E. Hilsenrath, G. W. Leppelmeier, G.B.J. van den Oord, P. K. Bhartia, J.
804 Tamminen, J. F. de Haan, and J. P. Veefkind, (2006) Science objectives of the Ozone
805 Monitoring Instrument, *IEEE Trans. Geosci. Remote Sensing*, 44, 1199–1208.

806 Martin, R. V., K. Chance, D. J. Jacob, T. P. Kurosu, R. J. D. Spurr, E. Bucsela, J. F. Gleason, P.
807 I. Palmer, I. Bey, A. M. Fiore, Q. Li, R. M. Yantosca, and R.B.A. Koelemeijer, (2002),
808 An improved retrieval of tropospheric nitrogen dioxide from GOME, *J. Geophys. Res.*,
809 107(D20), art. no. 4437.

810 Martin, R. V., B. Sauvage, I. Folkins, C. E. Sioris, C. Boone, P. Bernath, and J. Ziemke, (2007),
811 Space-based constraints on the production of nitric oxide by lightning, *J. Geophys. Res.*,
812 112, D09309, doi:10.1029/2006JD007831.

813 Ott L. E., K. E. Pickering, G. L. Stenchikov, H. Huntrieser, and U. Schumann, (2007), Effects of
814 lightning NO_x production during the 21 July European Lightning Nitrogen Oxides Project
815 storm studied with a three-dimensional cloud-scale chemical transport model, *J.*
816 *Geophys. Res.*, 112, D05307, doi:10.1029/2006JD007365.

817 Ott, L. E., et al., (2009), Production of lightning NO_x and its vertical distribution calculated from
818 3-D cloud-scale chemical transport model simulations, *J. Geophys. Res.*, in press.

819 Pickering, K., et al., (1996), Convective transport of biomass burning emissions over Brazil
820 during TRACE A, *J. Geophys. Res.*, 101(D19), 23993–24012.

821 Price, C., J. Penner, and M. Prather, (1997), NO_x from lightning, 1. Global distributions based
822 on lightning physics, *J. Geophys. Res.*, 102, 5929–5941.

823 Richter, A., and J. P. Burrows, (2002), Tropospheric NO₂ from GOME measurements, *Adv.*
824 *Space Res.*, 29, 1673.

825 Ridley, B., K. Pickering, and J. Dye, (2005), Comments on the parameterization of lightning-
826 produced NO in global chemistry-transport models, *Atmos. Environ.*, 39, 6184–6187.

827 Rodger C. J., S. W. Werner, J. B. Brundell, N. R. Thomson, E. H. Lay, R. H. Holzworth, and R.
828 L. Dowden, (2006), Detection efficiency of the VLF World-Wide Lightning Location
829 Network (WWLLN): Initial case study, *Ann. Geophys.*, 24, 3197–3214.

830 Rodger, C. J., J. B. Brundell, R. H. Holzworth, and E. H. Lay (2009), Growing Detection
831 Efficiency of the World Wide Lightning Location Network, *Am. Inst. Phys. Conf. Proc.*,
832 Coupling of thunderstorms and lightning discharges to near-Earth space: Proceedings of
833 the Workshop, Corte (France), 23-27 June 2008, 1118, 15-20, DOI:10.1063/1.3137706.
834 http://wwlln.net/publications/rodger_WWLLN_TLE_final_23Jan09.pdf

835 Schumann, U., and H. Huntrieser, (2007), The global lightning-induced nitrogen oxides source,
836 *Atmos. Chem. Phys.*, 7, 3823-3907.

837 Thornton, J. A., P. J. Wooldridge, and R. C. Cohen, (2000), Atmospheric NO₂: *In situ* laser-
838 induced fluorescence detection at parts per trillion mixing ratios, *Anal. Chem.*, 72, 528–
839 539.

840 Thornton, J. A., P. J. Wooldridge, R. C. Cohen, E. J. Williams, D. Hereid, F. C. Fehsenfeld, J.
841 Stutz, and B. Alicke, (2003), Comparisons of *in situ* and long path measurements of NO
842 in urban plumes, *J. Geophys. Res.*, 108, (D16), 4496, doi:10.1029/2003JD003559.

843 Tie, X., R. Zhang, G. Brasseur, L. Emmons and W. Lei, (2001), Effects of lightning on reactive
844 nitrogen and nitrogen reservoir species in the troposphere, *J. Geophys. Res.*, 106(D3),
845 3167-3178.

846 Tie, X., R. Zhang, G. Brasseur, and W. Lei, (2002), Global NO_x production by lightning, *J.*
847 *Atmos. Chem.*, 43, 61-74.

848 Toon, O. B., et al., (submitted, 2009), Planning and implementation of the Tropical Composition,
849 Clouds and Climate Coupling Experiment (TC⁴), *J. Geophys. Res.*

850 Wenig, M. O., A. M. Cede, E. J. Bucsela, E. A. Celarier, K. F. Boersma, J. P. Veefkind, E. J.
851 Brinksma, J. F. Gleason, and J. R. Herman, (2008), Validation of OMI tropospheric NO₂
852 column densities using direct-sun mode Brewer measurements at NASA Goddard Space
853 Flight Center, *J. Geophys. Res.*, 113, D16S45, doi:10.1029/2007JD008988.

854 Zhang X., J. H. Helsdon Jr., and R. D. Farley, (2003), Numerical modeling of lightning-produced
855 NO_x using an explicit lightning scheme: 2. Three-dimensional simulation and expanded
856 chemistry, *J. Geophys. Res.*, 108(D18), 4580, doi:10.1029/2002JD003224.

857 Zhang, R., X. Tie, and D. W. Bond, (2003) Impacts of anthropogenic and natural NO_x sources
858 over the U. S. on tropospheric chemistry, *Proc. Natl. Acad. Sci. U. S. A.*, **100**, 1505 –
859 1509.

860

861

861 **Figure Captions**

862

863 **Figure 1:** DC-8 flight tracks in the vicinities of storms sampled on (a) July 17, (b) July 21, (c)
864 July 31, and (d) August 5, 2007 during the TC⁴ mission superimposed on Geostationary
865 Operational Environmental Satellite (GOES-10/12) color-enhanced infrared images. Insets show
866 the pressure altitude during flight.

867

868 **Figure 2:** Profiles involved in AMF calculations in this study, (a) r_{BG} = background NO_2 , $r_{L\text{NO}_2}$ =
869 lightning NO_2 , (b) a = atmospheric scattering weight, β = temperature correction factor, γ = three
870 profiles representing the $[\text{NO}_x]/[\text{NO}_2]$ ratio. The profiles $r_{L\text{NO}_2}$ and r_{BG} are fixed. All others
871 depend on pixel location (typical examples are shown here).

872

873 **Figure 3:** OMI effective geometrical cloud fraction (at the time of OMI overpass) on the four
874 dates in this study (a) July 17, (b) July 21, (c) July 31, and (d) August 5, 2007. The polygons
875 outline regions examined for enhanced NO_2 due to lightning.

876

877 **Figure 4:** Vertical column densities of LNO_x inferred from OMI data, for (a) July 17, (b) July
878 21, (c) July 31, and (d) August 5, 2007. The polygons outline regions examined for enhanced
879 NO_2 due to lightning.

880

881 **Figure 5:** Corrected stratospheric field, estimated from OMI data for July 21, 2007 (a) using the
882 planetary-wave analysis up to wave-2, and (b) using the PRS method. Both fields have been

883 corrected by subtracting a model GMI tropospheric background, equal to approximately 5% of
884 the stratospheric column value.

885

886 **Figure 6:** OMI tropospheric NO₂ background averaged over data 5 days of minimal convective
887 activity in July and August 2007.

888

889 **Figure 7:** Mean LNO_x production, P_{IC+CG}, for all lightning flashes produced by storms analyzed
890 in TC⁴, compared with those of previous studies. Colors indicate approximate wind speeds in the
891 upper troposphere.

892

893 **Figure 8:** . LIS (a) flash rate density (flashes km⁻² s⁻¹) and (b) event rate density (events km⁻² s⁻¹),
894 gridded in 0.1° × 0.1°, prior to the OMI overpass, on the July, 21, 2007 case. The light gray
895 shaded area corresponds to LIS field of view during this orbit passage. Frequency of occurrence
896 of flash footprints during LIS observations of (c) the July, 21, 2007 case, and (d) 2007 boreal
897 summer (June, July, August – JJA).

898

899

900

900 **Tables**

901

902 **Table 1:** Summary of LNO_x measurement results.

903

Date	Region	Area (10 ³ km ²)	300 hPa Winds (Direction, m/s)	LNO _x (kmol)	Lightning Flashes	P _{IC+CG} (mol/flash)
July 17	South of Panama/CR	160	ENE 4	430	4931	87 ± 252
July 21	NW coast of Colombia	194	W 2 (north side) E 2 (south side)	2765	20515	135 ± 114
July 31	SW of Costa Rica	478	E 8	3490	14190	246 ± 287
August 5	W coast of Colombia	246	NE 14	2363	10388	227 ± 223

911

912

913 **Table 2a:** LNO_x in each region and contributions to the error budget.

914

Date	Value (kmol)	Statistical Error (kmol)	Strat,Trop, and profile Error (kmol)	Region-selection Error (kmol)	Combined Error (kmol)
July 17	430	±419	±1149	±162	±1234
July 21	2765	±557	±2037	±104	±2114
July 31	3490	±778	±3828	±1008	±4034
August 5	2363	±508	±1986	±650	±2151

921

922

923 **Table 2b:** LNO_x and flash-count errors and their contribution to production-efficiency error.

924

Date	LNO _x (kmol)	Lightning Flashes (IC + CG)	LNO _x Production P _{IC+CG} (mol/flash)
July 17	430± 1234	4931 ± 1775	87 ± 252
July 21	2765± 2114	20515 ± 7385	135 ± 114
July 31	3490± 4034	14190 ± 2129	246 ± 287
August 5	2363± 2151	10388 ± 3740	227 ± 223

931

932

933 **Table 3:** Lightning NO_x enhancement factors

934

935

Date	NO _x (pptv) DC-8 in-cloud	NO _x (pptv) DC-8 clear sky	Enhancement Factor (DC-8)	OMI LNO _x . (10 ¹⁵ cm ⁻²)	NO _x Background (10 ¹⁵ cm ⁻²)	Enhancement Factor (OMI)
July 17	110	60*	1.83	0.16	0.81	1.20 ± 0.6
July 21	538	309	1.74	0.86	2.38	1.36 ± 0.3
July 31	876	375	2.34	0.44	1.10	1.40 ± 0.5
Aug 5	357	152	2.35	0.58	1.37	1.42 ± 0.4

942

943

944

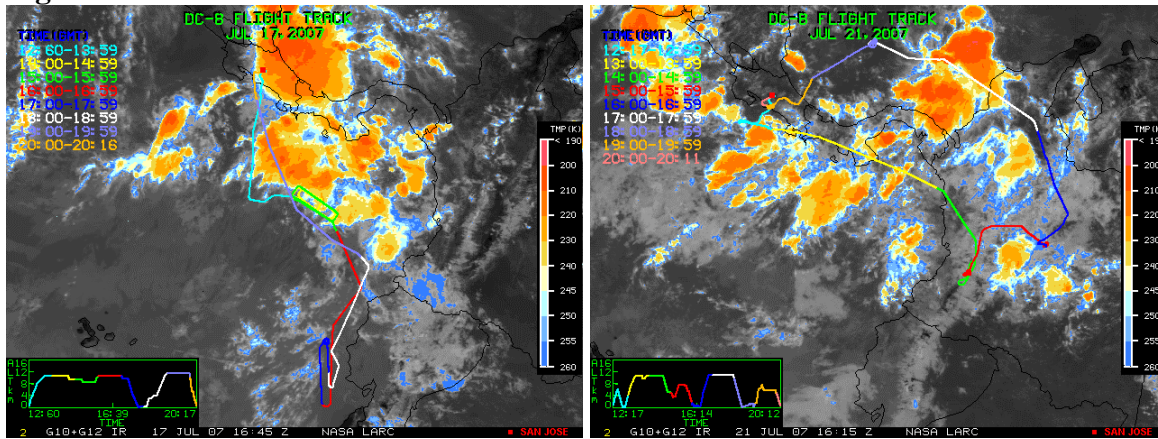
945

*Taken from GMI model because of a lack of clear-sky observations unaffected by storm outflow or pollution plumes

945 **Figures**

946

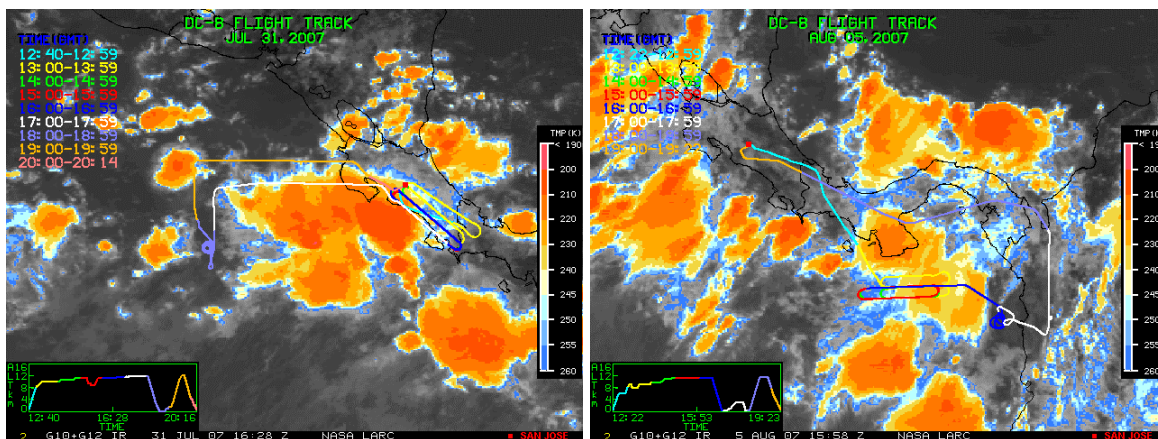
947 **Figure 1**



948

949 (a)

(b)



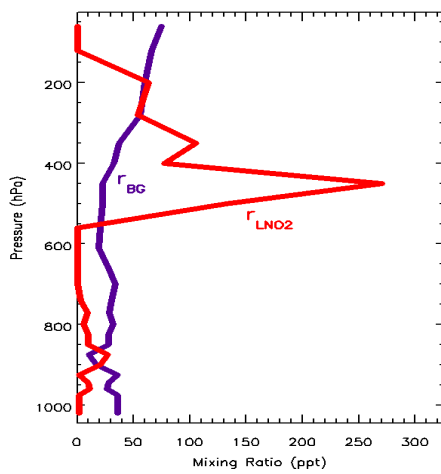
950

951 (c)

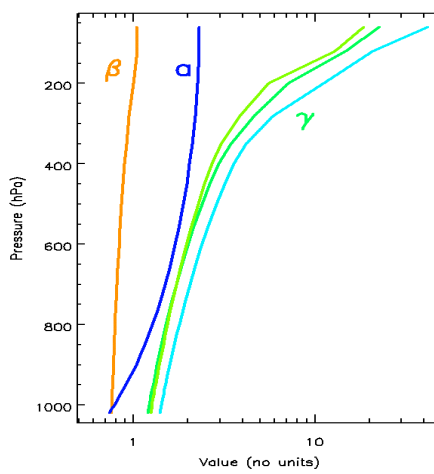
(d)

952 **Figure 2**

953



(a)



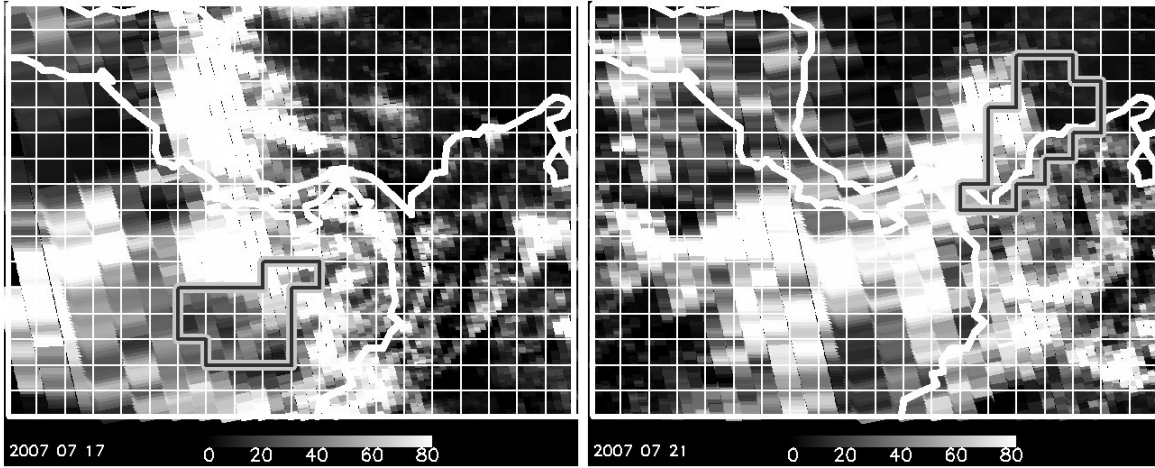
(b)

954

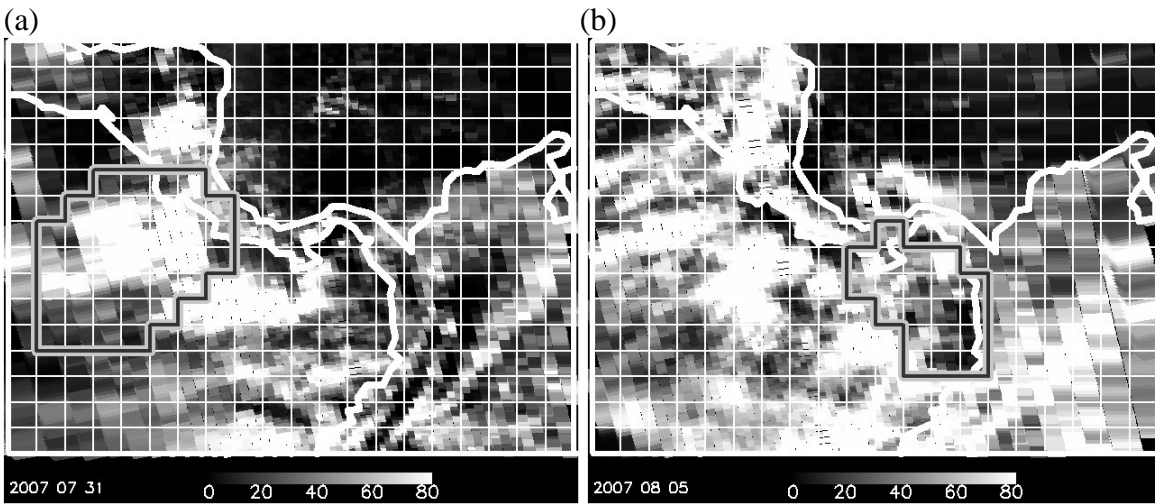
955

955
956

Figure 3



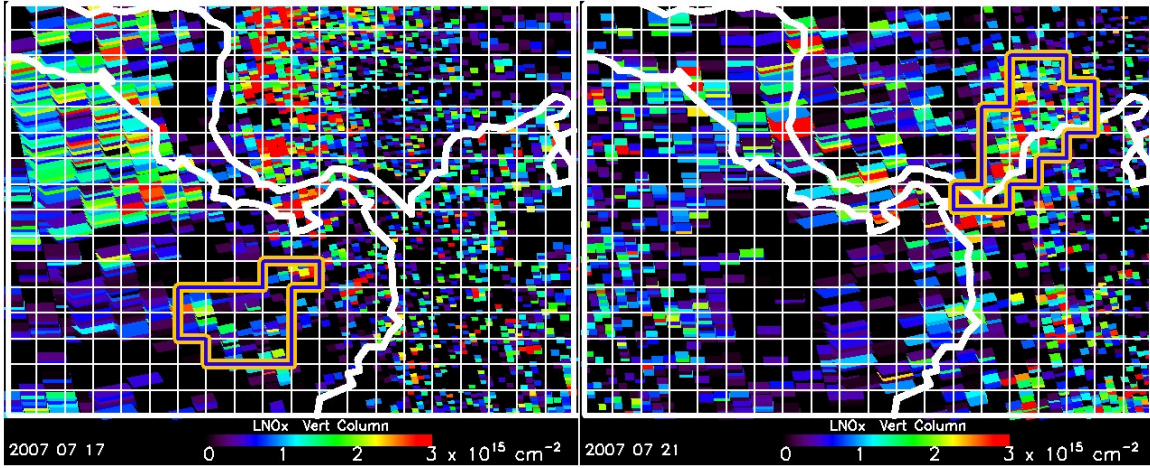
957
958



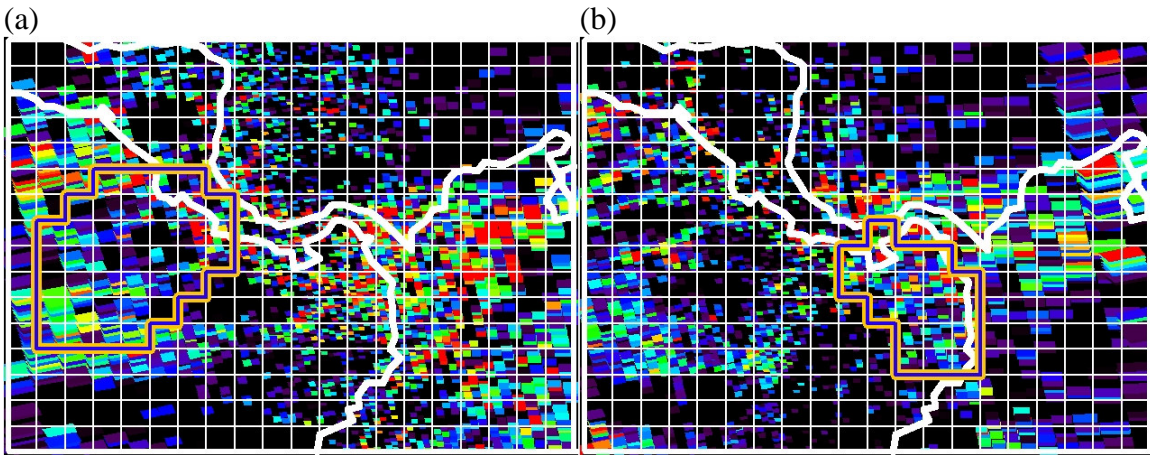
959
960
961

961
962

Figure 4



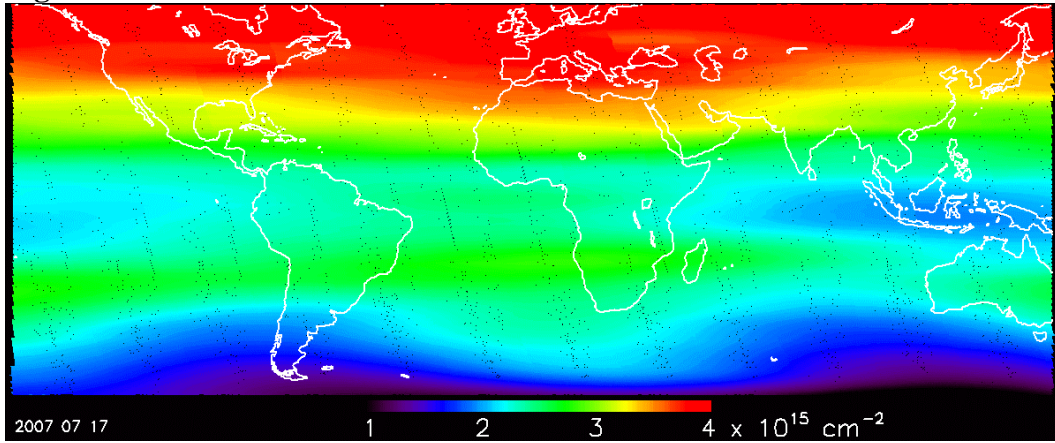
963
964



965
966
967
968

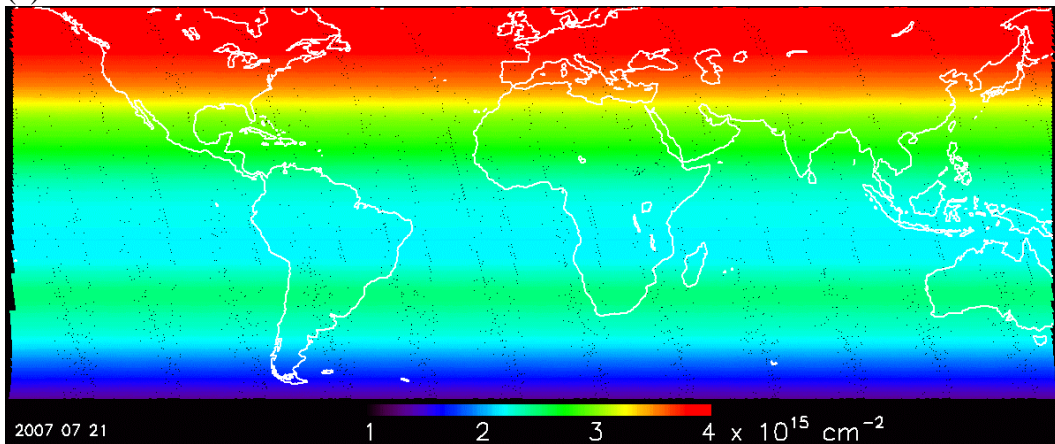
968
969
970

Figure 5



971
972

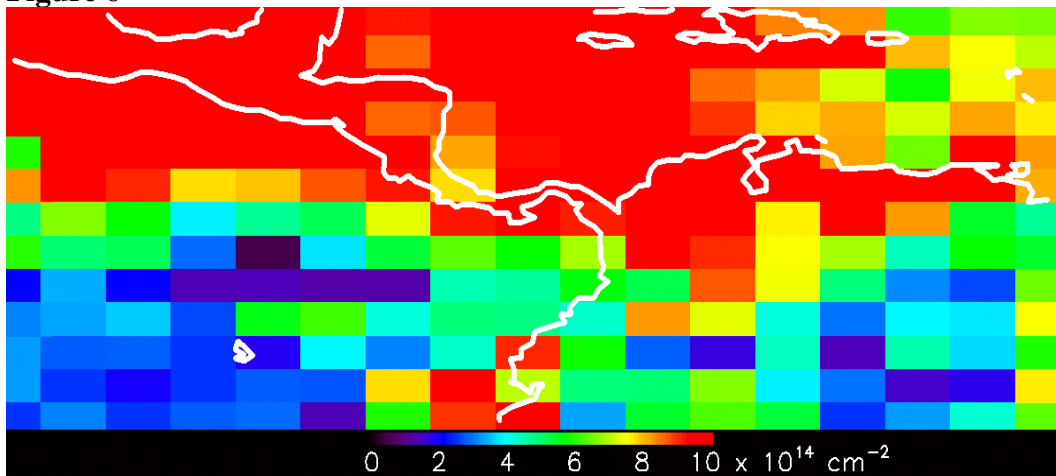
(a)



973
974
975

(b)

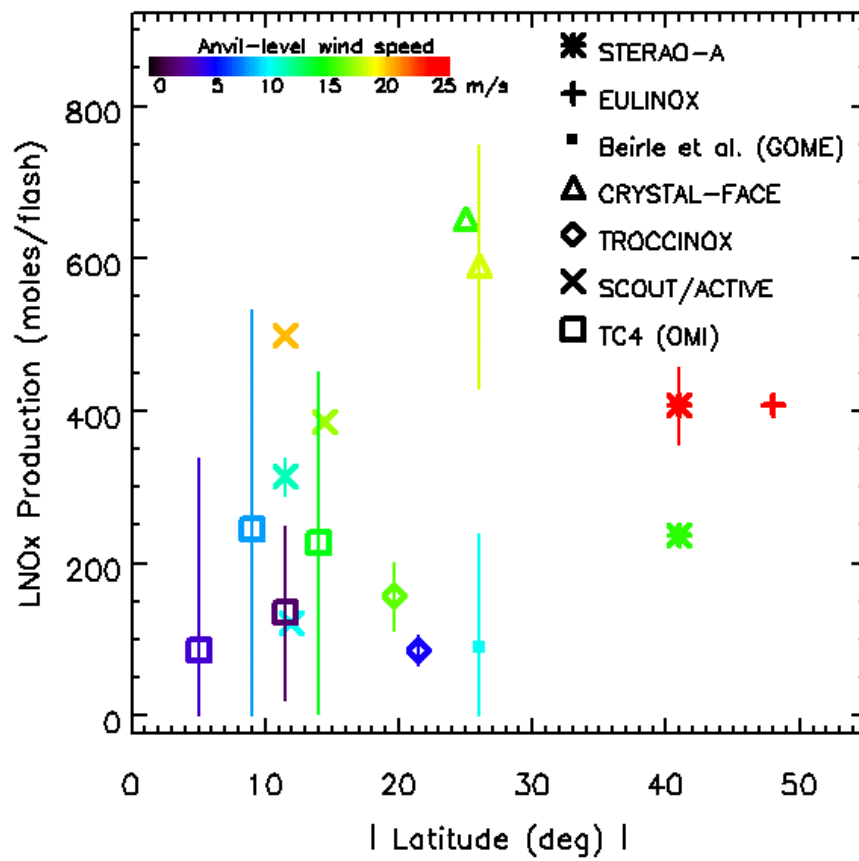
975 **Figure 6**



976

977

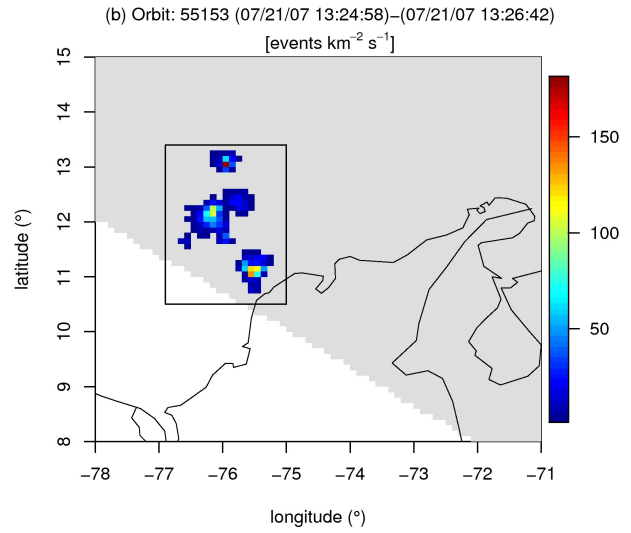
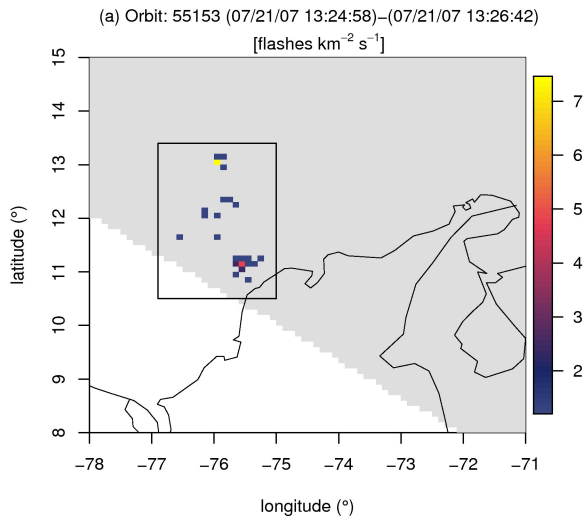
978 **Figure 7**



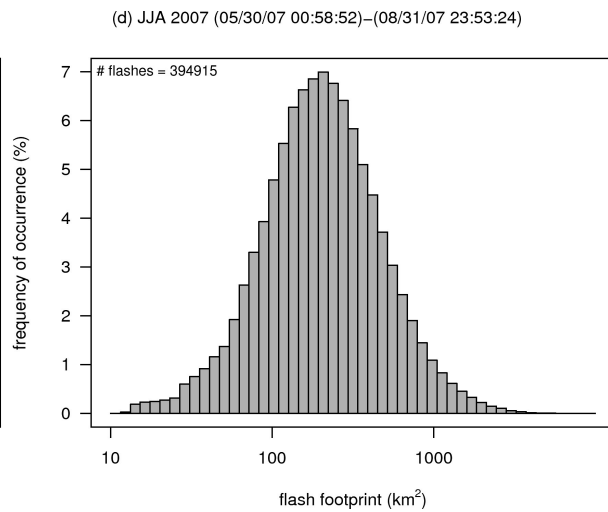
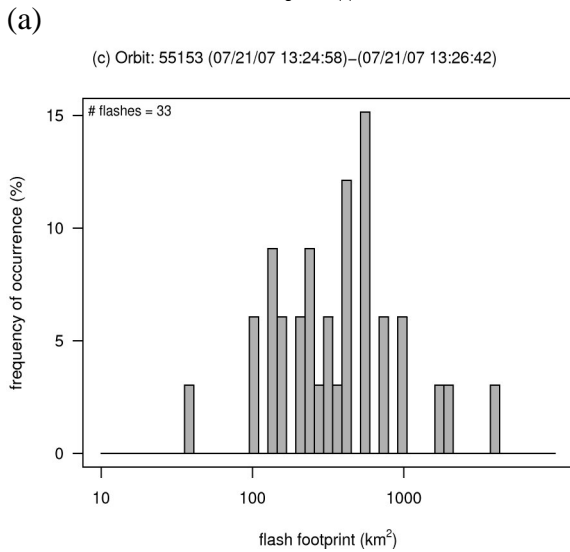
979

980

980 **Figure 8**
981



982
983



984
985
986